Powder Technology 354 (2019) 584–590 https://doi.org/10.1016/j.powtec.2019.06.033

Determining the density distribution in cemented carbide powder compacts using 3D neutron imaging

Hjalmar Staf [a,b], Zoltán Kis [c], László Szentmiklósi [c], Bartek Kaplan [b], Erik Olsson [a] and Per -Lennart Larsson [a,*]

[a)] *Department of Solid Mechanics, KTH Royal Institute of Technology, SE-100 44, Stockholm, Sweden*

[b)] *Sandvik Coromant, SE-126 80, Stockholm, Sweden*

[c)] *Centre for Energy Research, Hungarian Academy of Sciences, HU-1121, Budapest, Hungary*

Abstract

Spray-dried refractory carbide and metal powder mixtures, containing tungsten carbide, is compacted and sintered during the production of conventional cutting tool inserts. Since friction between the pressing tool and the powder gives rise to density gradients in the powder compact, shrinkage during sintering is uneven. The shape of the sintered blank is important and can be predicted with finite element (FE) simulations. To validate the simulation of the pressing procedure, the density gradients in the powder compacts must be measured with a high spatial resolution. Since tungsten has a high atomic number, it is hard to penetrate with X-rays and even cold neutrons. We show here that using a polychromatic beam of thermal neutrons, along with beam-hardening correction, such measurements can be successfully realized. The obtained results show good agreement with corresponding FE-simulations. Also, deliberate differences in the compaction process could be verified with the neutron measurements.

1 Introduction

Metal-powder compaction and sintering is a widely used industrial process with the advantage of high productivity and good net shape. After compaction, where the powder is pressed in a pressing tool, the powder compact is sintered to full density. Conventional cutting tool inserts, used for machining of various materials, are produced with a spray-dried refractory carbide and metal powder mixture, the main ingredients being tungsten carbide, cobalt, and a pressing agent, in this case, PolyEthylene Glycol (PEG). The sintered cutting insert blanks are often ground and coated before they are used in a machining operation.

Cemented Carbide is well suited for cutting inserts since it has a high hardness together with some ductility. The shape of the insert is crucial for its performance, and therefore, very important to consider in the design process [1]. During powder compaction, the cemented carbide powder is pressed to roughly half of its original volume. Friction between the pressing tool and the powder gives rise to density gradients in the powder compact [2]. During sintering, the uneven density results in uneven shrinkage, making it difficult to predict the shape after pressing and sintering to the desired accuracy. To obtain the correct shape of the sintered blank,

*Corresponding author

Email addresses hjalles@kth.se (Hjalmar Staf), kis.zoltan@energia.mta.hu (Zoltán Kis), szentmiklosi.laszlo@energia.mta.hu (László Szentmiklósi), bartek.kaplan@se.aga.com (Bartek Kaplan), erolsson@kth.se (Erik Olsson) and plla@kth.se (Per-Lennart Larsson)

the pressing tool must, therefore, be compensated for which knowledge of the density gradient in the powder compact is crucial.

By doing FE-simulations of the compaction and sintering process, the pressing tool can be compensated before it is manufactured [3]. This has proven to be a useful design tool that saves time and money in the development phase of new cutting tool insert geometries. The complete simulation process can easily be verified by comparing the shape after sintering, but to validate the compaction simulation it is important to measure the density gradient in the powder compact.

FE-simulation of powder compaction to high density is mostly treated phenomenologically, assuming a porous solid and using, for example, a Gurson model [4], a CamClay model [5] or a Drucker-Prager CAP model [6]. Here a material model that can be described as an extended Drucker-Prager CAP model, suggested by Ref. [7], with material parameters presented in [8], is used. The model is complex with many material parameters, such as a density-dependent yield surface. Previous research with an instrumented pressing tool, together with reverse engineering, gave useful but insufficient data for a complete set of material parameters [9]. A sensitivity study of the material model showed that the density after pressing is an important variable when defining the material parameters [10,11]. The present measurements are thus of high importance for characterization of the material used in the FE-simulations.

Various methods are available for density-gradient measurements in powder compacts. In [12] and [13] the surface hardness is measured with indentation and scratch testing, and used to calibrate to a local density. When the density inside the powder compacted is needed, this method requires destructive cutting of the compact, which itself could influence the surface properties. Furthermore, an accurate interpretation of such experiments is difficult at best. Powder behavior during compaction and local density in powder compacts can be analyzed with small-angle X-ray scattering (SAXS) as demonstrated in [14–16]. Also, computed tomography (CT) has been used (X-rays) [17] as well as ultrasound techniques [18]. The main issue with X-ray-based methods, when measuring compacts made of tungsten carbide powders, is the low penetration depth due to the high atomic number of tungsten. Consequently, they are inapplicable to reliable volumetric measurements, even when using cold (lower energy) neutrons, the penetration is too low [19]. One workaround of the low penetration could be to substitute WC with MoC since both have the same lattice structure [20]. Of course, it is more direct and with lower risks of error to measure the real powder material. Since the density difference is comparatively small within the compact (±10-20%), the measurement must be accurate, which of course makes the approach even more challenging.

In the present work, polychromatic thermal neutrons are used to probe the density gradient in powder compacts containing WC. FE-simulations of the compaction process will be used to validate the results and such a combined approach has, to the author's knowledge, never been presented previously for hard metal powders with a successful outcome. The usefulness of the procedure for material characterization will be discussed. Furthermore, the measurements will also be used to verify the effect of different compaction methods, discussed in previous research and presented in [2]. In this study, it was shown that the pressing speed and not the holding time, related to creep effects, influences the shape after sintering. This indicates that the density gradient is affected by the pressing speed. In [21] it was shown that the pressing speed influences wall friction, which could explain this behavior. The relaxation that occurs during holding, before the press punch is released [2], is believed not to be an effect of creep since the shape after sintering is not affected. This will be confirmed presently by recording the density gradient in samples compacted with different holding time.

2 Test Specimens

Powder compacts, both real cutting tool geometries as well as calibration samples with uniform densities, were produced as described in Section 1. All samples are produced from the same cemented carbide powder raw material, which is a WC-Co mixture containing roughly 88 % WC, 10 % Co together with 2 % PEG (measured in weight). It is a spray-dried refractory carbide and a metal powder mixture of the same type as used in previous research [1,3,8,11,21]. The WC and Co particles have a representative size of approximately 1 μm, while the corresponding size for the granules, after spray-drying, is in the order of 100 μm. The average relative density is 55 % after compaction (measured relative to sintered density). The pressing agent Polyethylene Glycol (PEG) contains hydrogen, resulting in severe scattering of neutrons, which will be discussed later. With the assumption that only PEG 300 (300 g/mol) is used, which is a slightly conservative assumption, 2 % PEG means approximately 10^{22} H-atoms/cm^3.

The powder compact is a so-called cross-hole geometry. The axis of the central hole is perpendicular to the compaction direction, which leads to higher density differences compared to the simpler geometries. Figure 1 shows a drawing of the powder compact, pressed with an upper and lower punch from top and bottom in the picture. A sensitivity study presented in [11] shows that this geometry activates different parts of the material model presently used for simulation purposes and presented below.

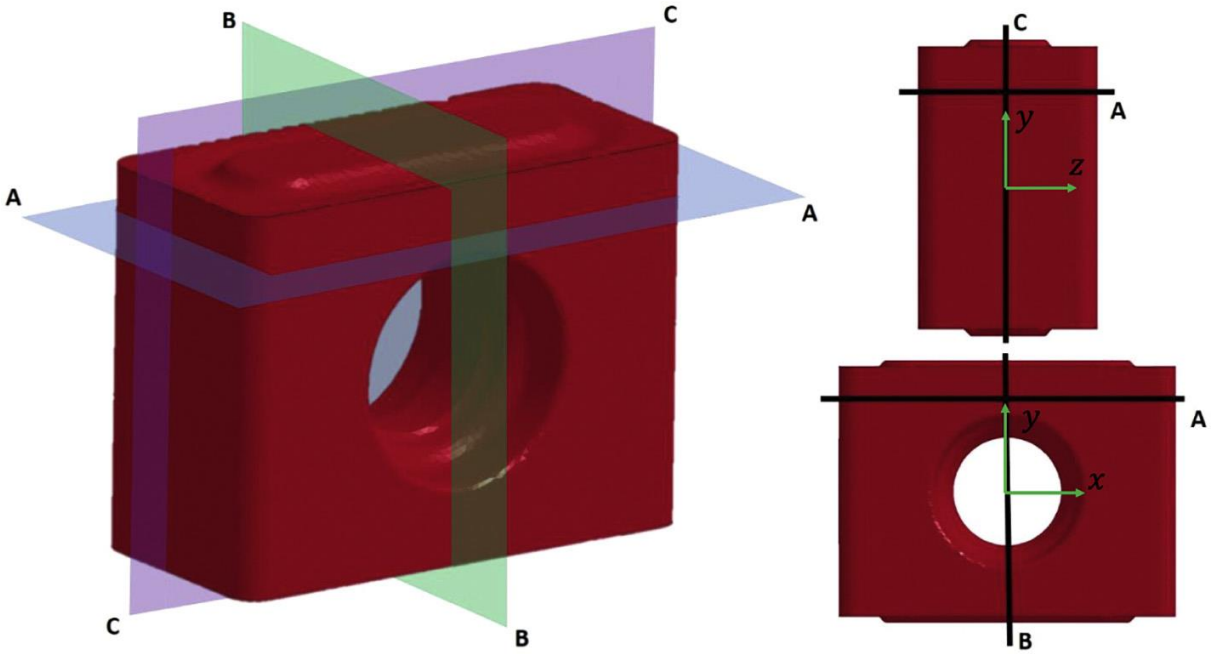

Figure 1: Geometry of powder compact measured and simulated currently. Compacted with an upper and lower punch (top and bottom in picture). A, B and C defines planes later used to present the result. The compaction direction is perpendicular to plane A.

Three versions of the mentioned powder compact, compacted using slightly different procedures, are measured, marked with I, II and III. As seen in Table 1, holding time after compaction and pressing speed have been varied. The effect of these variations has been analyzed in [2] and discussed in Section 1.

Version	Weight	Pressed height	Pressing speed	Holding time
Compact I	13.176 g	13.992 mm	1 mm/s	80 ms
Compact II	13.176 g	13.991 mm	25-75 mm/s	80 ms
Compact III	13.175 g	13.989 mm	25-75 mm/s	1000 ms

Table 1: Pressing details for powder compacts measured. Details are explained in previous research [2].

For beam hardening correction, and in order to establish a correspondence between the local attenuation and local density, reference samples with uniform densities were produced in a dry-bag press (isostatic press) [22]. A cylinder was compacted and cut into different heights (2.5, 5, 10 and 20 mm). It is believed that the density in this set of samples is uniform since the pressure during compaction is equal all over the outer surface.

3 Test Setup and Data Evaluation

Density gradient measurements of the powder compacts were performed at the neutron imaging facility (RAD) of the Budapest Neutron Centre, using a beam of thermal neutrons [23]. As shown in the schematic radiography setup, **Error! Reference source not found.** the sample was placed in the polychromatic thermal neutron beam in front of a 200 µm thick ZnS/^{6}LiF scintillation screen. Behind the screen, a 45-degree mirror and an Andor Neo sCMOS camera with an *f*105 lens are mounted to produce 16–bit grayscale images. For the present measurements, the exposure time is 23 s per image. This way the full dynamic range of the 16-bit grayscale was used and saturation of pixels was avoided. Neutron radiograms (NR) represent the integral of the attenuation throughout the sample [24]. During tomography, a set of radiographic images, the so-called projections, is acquired as the object is incrementally rotated. We used 1126 angular positions throughout the 360° full turn, which is close to the ideal number (1490) to reach the theoretically achievable spatial resolution for the setup. The spatial resolution was 270 µm, and the acquisition time for a full tomography was seven hours. The explicit value on the resolution indicates that, considering the sizes of the individual particles, that the measurements will give an average description of the powder compact and any inhomogeneity cannot be effectively resolved. To avoid the influence of scattered neutrons, mainly due to hydrogen in PEG, the sample is placed 50 mm away from the screen (object-to-screen distance). Considering the number of H-atoms in the samples and the isotropic scattering angle of the neutrons, this is a practical way to avoid image bias [25].

From this data, a 3D volume can be reconstructed using computational algorithms [26,27], showing the local attenuation property at every 3D point. The image processing and analysis were performed using FIJI [28], Octopus [29], VGStudio MAX [30] and KipTool [31] software packages.

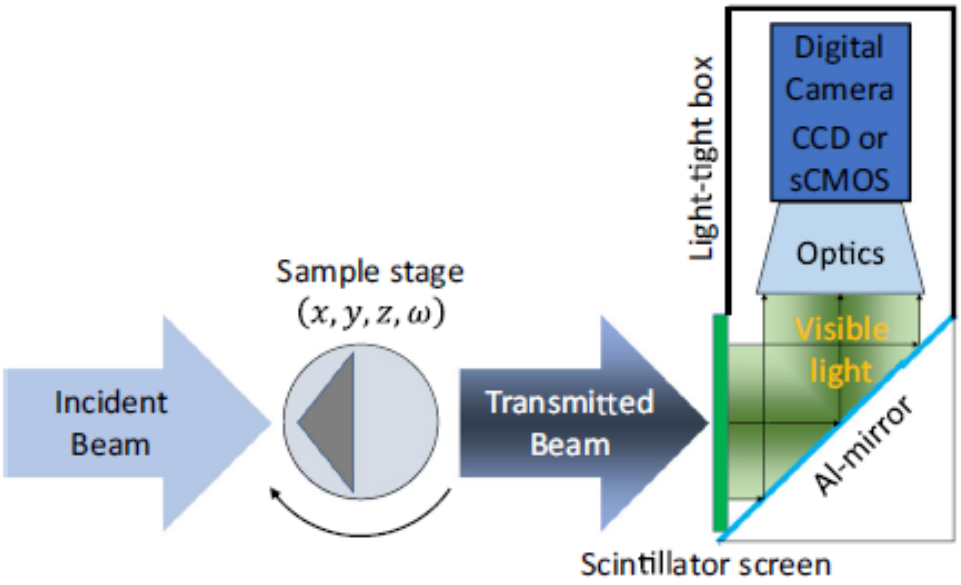

Figure 2: A typical radiography setup consisting of a neutron sensitive, visible-light emitting scintillator screen, a mirror, optics and a digital camera. The sample is put in front of the screen for radiography and rotated by a sample stage for tomography.

The simplest form of the Beer-Lamberts attenuation law for the transmitted neutron intensity is as follows:

$$\frac{I}{I_0} = e^{-\Sigma d} \tag{1}$$

where I is the intensity of the transmitted beam, I_0 the incident beam intensity, d the material thickness and Σ the linear attenuation coefficient. This law - strictly speaking - is valid only in homogeneous materials and if the detector is point-like, there is a well-collimated, mono-energetic pencil beam, and the so-called build-up effect can be neglected. When there are regions with different attenuation effects in the path of the neutron beam, it can theoretically be represented by the following integral quantity:

$$\frac{I}{I_0} = e^{-\int_{beam\ path} \Sigma(\vec{r}) ds} \tag{2}$$

where $\Sigma(\vec{r})$ is the local linear attenuation coefficient. The latter quantity can be reconstructed from the neutron tomography experiment and, as it correlates with the local density for a given material, is the quantity we presently like to measure. Unfortunately, there is a serious beam hardening effect, which biases the measured raw values of the local linear attenuation coefficients. In the next paragraphs we describe how the beam hardening effect could be corrected for using a set of homogeneous reference samples (described in Section 2).

The attenuation constant for a given material Σ (macroscopic quantity) depends on the local atomic density and the local energy distribution of the neutrons via the interaction probabilities of the neutron absorption and scattering. The linear attenuation coefficient can be related to microscopic quantities as

$$\Sigma = \rho_a(\sigma_{abs} + \sigma_{scat}) \quad (3)$$

where ρ_a is the atomic density, σ_{abs} is the absorption cross-section and σ_{scat} the scattering cross-section.

During the 3D reconstruction, the projections are used to produce the map of the linear attenuation coefficient, Σ, in the horizontal slices of the object [26]. The reconstructed slices, however, have to be corrected for the so-called beam hardening effect, if it is not negligible. Beam hardening means that lower-energy neutrons in the beam tend to be absorbed more likely already closer to the surface than higher energy ones, as they traverse through a layer of matter, since the neutron attenuation probability increases with decreasing neutron velocities. The consequence is a less intense but more energetic beam, for which the mean free path in the sample is larger, and its transmission is higher. In the reconstructed tomographic slices, it appears as if the middle region of a slice would be more transparent (lower apparent Σ values), showing a cup-like artifact along a line profile.

The reference samples were explained in Section 2. "Test Specimens" and measured in the length direction as shown in Figure 3, were used to establish a suitable function for the beam hardening correction. As Σ depends on both the local energy-distribution of the neutrons (via the cross sections), and the local density of the material, the magnitude of the beam hardening can therefore be measured using a series of homogeneous samples with a constant density but different thicknesses, i.e. our reference samples. In this case, the change in the linear attenuation coefficient is attributed solely to the energy-dependent cross section values. Tallying this change for various thicknesses will provide the correction function for beam hardening.

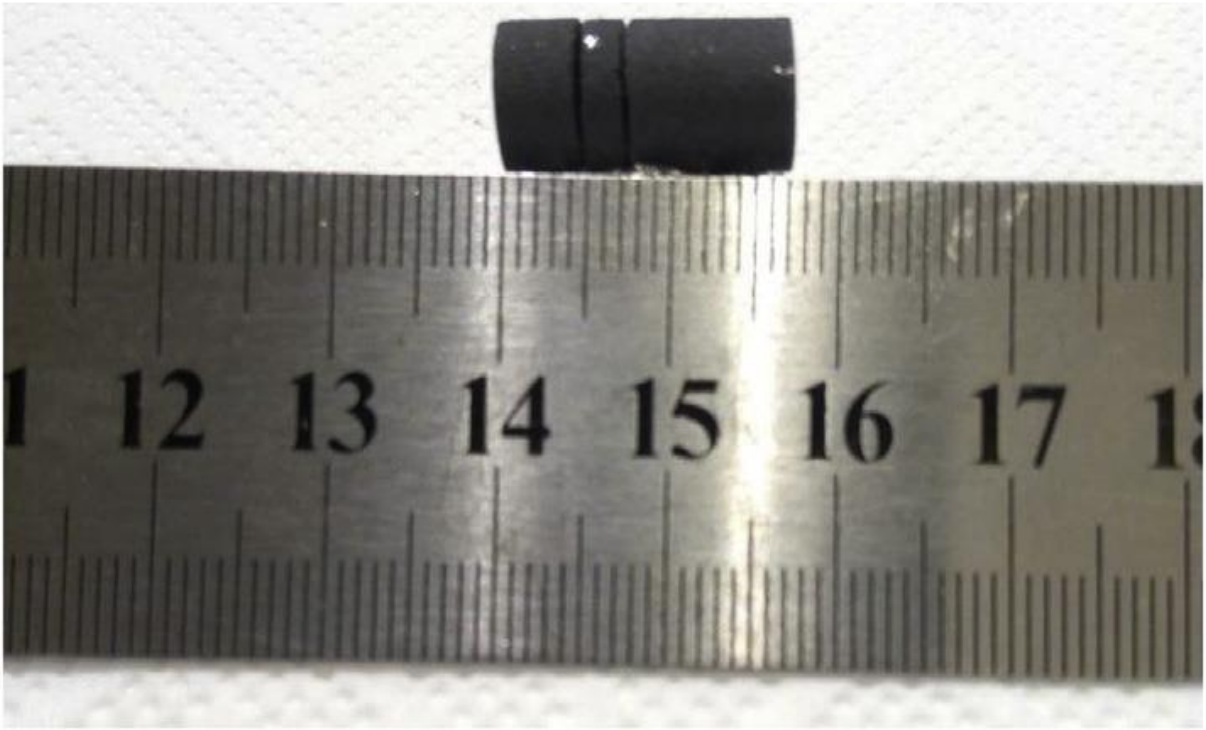

Figure 3: Reference samples with different thicknesses mounted in front of screen for measurement.

Beam hardening correction (BHC) of the reconstructed slices was carried out using the appropriate function in the Octopus tomographic reconstruction code [29]. The attenuation function is of course only valid for the current samples (with the specific chemical composition), up to the maximum calibrated thickness, in the current measurement geometry and at this specific neutron-energy distribution of the RAD facility. To determine the BHC function three simple types of functions, a linear, a quadratic and a double exponential were selected. The linear function assumes no BHC, it was involved just for the aim of comparison. The quadratic and double exponential functions are standards used in the beam hardening calculations [32].

$$\Sigma d = a_1 d \tag{4}$$

$$\Sigma d = b_1 d + b_2 d^2 \tag{5}$$

$$\Sigma d = -\ln\left[c_1 + c_2 \exp\left(-\frac{d}{c_3}\right) + c_4 \exp\left(-\frac{d}{c_5}\right)\right] \tag{6}$$

The functions were fitted to measured data points. As seen Figure 4 the best fitting was reached by using the double exponential function Eq. (6), in the thickness range of 0 – 35 mm.

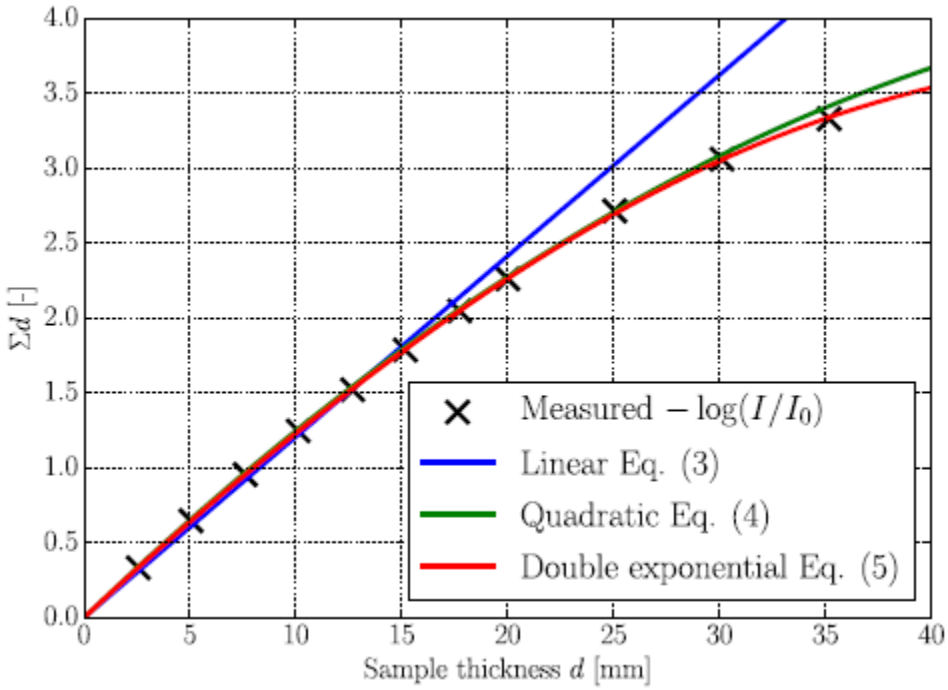

Figure 4: Measured attenuation multiplied with sample thickness (Σd) plotted against samples thickness d together with the three beam hardening correction equations, Eq. (4) – Eq. (6).

Once the linear attenuation coefficient Σ is corrected for beam hardening, it is assumed that Σ has a linear relation to the atomic density ρ_a. This means that a calibration function between the measured local attenuation values of the object and its local mass density ρ_m can be written as

$$\rho_m = \rho_a \frac{M}{N_{Av}} = c_s \Sigma \tag{7}$$

where M is the atomic weight, N_{Av} is Avogadro's number and c_s is a scaling parameter. To determine the slope c_s of the calibration line, the mass density and the corresponding linear attenuation coefficient must be known for a homogeneous object. The value of Σ comes from the BH-corrected neutron tomographic measurements. The density value was derived from the sample, mass measured using a balance and the volume of the object, calculated from the tomography results based on the number of the voxels belonging to the object. The accuracy of the dimensions measured on the NT images with VGStudio MAX was validated by independent measurements of the same dimensions using a caliper.

Based on the BH-corrected tomographic slices an average linear attenuation value was calculated for the homogeneous samples. The result revealed that even these samples are not perfectly homogeneous. However, the inhomogeneity is less than ±1.5%. The fit of the average attenuation against the corresponding average densities, shown in Table 2 yielded $cs = 8.76\ \mathrm{g/cm^2}$. This relationship was used to calculate the density gradient for the powder compacts with insert geometry. Beam-hardening-corrected tomograms of the powder compact, multiplied by its corresponding c_s, gives a 3D map of the true local density.

Height of reference sample	**2.5 mm**	**5 mm**	**10 mm**	**20 mm**	**Average**
Density (g/cm³)	8.12	8.13	8.18	8.12	8.14 ±0.03

Table 2: Data for reference samples used to determine the relation between local density and attenuation.

4 FE Simulation

The FE-simulation relies on a material model for powder compaction used in previous research regarding the same powder material [2,8,11], and was first presented by Brandt [3]. It is an elastic-plastic model with a yield surface of Drucker-Prager CAP kind. The yield surface is described by an elliptic CAP part f^{CAP} and a quadratic failure curve $f^{failure}$.

$$f^{CAP}(d,\ I_1,\ J_2) = \sqrt{J_2} - \frac{1}{R}\sqrt{[L - X(d)]^2 - [L - I_1]^2} = 0 \tag{8}$$

$$f^{failure}(d,\ I_1,\ J_2) = \sqrt{J_2} - c_0(d) + \ c_1(d) I_1 + c_2(d) I_1^2 = 0 \tag{9}$$

In Eqs. (8) and (9), I_1 is the first invariant of the Cauchy stress tensor, σ_{ij}, giving $I_1 = \sigma_{ii}$ and J_2 is the second invariant of the stress deviator, $s_{ij} = \sigma_{ij} - 1/3 I_1 \delta_{ij}$, giving $J_2 = s_{ij} s_{ij}$. The size of the CAP part is determined by the yield point in hydrostatic compression, $X(d)$, which is a function of the relative density, d, defined as the density of the compacted powder divided

by sintered density. The shape is controlled by two parameters, L and R. Furthermore, the failure part of the yield surface, $f^{failure}$, is described by three density dependent functions as

$$c_0(d) = -Y(d)\frac{\left[\frac{L^2}{\sqrt{3}} - \frac{L - X(d)}{R}(Y(d) - 2L)\right]}{[L^2 + Y(d)(Y(d) - 2L)]} \tag{10}$$

$$c_1(d) = -2L\frac{\left[\frac{L^2}{\sqrt{3}} - \frac{L - X(d)}{R}\right]}{[L^2 + Y(d)(Y(d) - 2L)]} \tag{11}$$

$$c_2(d) = \frac{c_1(d)}{2L} \tag{12}$$

These functions result in a smooth yield surface at the transition point $I_1 = L$ while giving that the yield stress at uniaxial compression becomes $Y(d)$, which controls the size of this part of the yield surface. The yield stress at pure shear becomes $c_0(d)$, as a result of Eq. (9). The direction of the plastic strains is given as an offset angle, φ, from the associative flow direction which is a function of the ratio between the volumetric and deviatoric stresses as

$$\varphi = \varphi\left(\frac{I_1}{X(d)}\right) \tag{13}$$

The yield surface for a relative density of $d = 0.55$, including a visualization of the direction of the plastic strains, is presented in Figure 5 (a), with a magnification of the region around $I_1 = 0$ in Figure 5 (b).

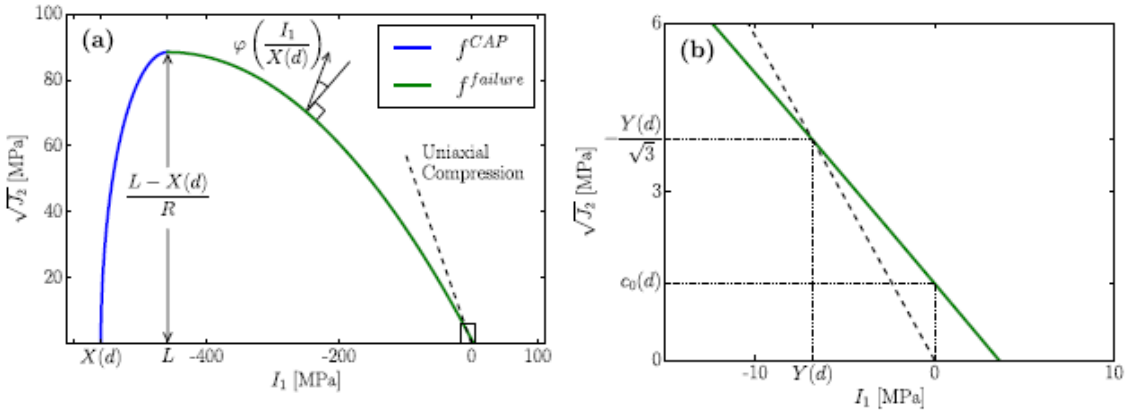

Figure 5: (a) Visualization of the yield surface for the used material model developed by Brandt [3]. (b) Magnified view of the marked area in (a) showing the region around $I_1 = 0$.

Anisotropy is included in the original model by Brandt in terms of kinematic hardening. However, a recent sensitivity study in the literature [11] shows that this effect has a rather small

influence on the density distribution in the compact. For this reason, anisotropy is presently neglected in the simulations.

The hyperelastic behavior is assumed to be isotropic and described by a density-dependent bulk modulus, $K(d)$, and Poisson's ratio ν. The parameters for the yield surface, $L/X(d)$ and R, Poisson's ratio and the initial relative density are presented in Table 3. The 4 presently needed material functions $K(d)$, $X(d)$, $Y(d)$ and $\varphi(I_1/X(d))$ are given graphically in [2].

Parameter	$\boldsymbol{\nu}$ **[-]**	$\boldsymbol{d_0}$ **[-]**	$\boldsymbol{L/X(d)}$ **[-]**	$\boldsymbol{R}$ **[-]**
Value	0.37	0.35	0.82	1.14

Table 3: Values of the material parameters in the constitutive model which were determined in [8].

The FE simulations are performed using the commercial software LS-Dyna [33] with explicit integration. The meshed powder compact consists of 200 000-300 000 one-point tetrahedron elements and remeshing is performed during the compaction process. Problems with shear locking are minimized by the remeshing procedure. The material model discussed above is implemented in LS-Dyna [34] and used in the simulations. Pressing tools are assumed to be rigid, and modeled with shell elements, and the frictional contact is described by the Coulomb friction law,

$$\tau = \mu_f p \tag{14}$$

where p is normal pressure, τ is shear stress and μ_f is the frictional coefficient determined to 0.2 in [35].

5 Results

A detailed evaluation of the 3D imaging datasets provided local density values in the powder compacts containing tungsten carbide. The effect of beam hardening is handled with the correction curve Eq. (6), determined from reference samples. Tomographic slices were corrected for beam hardening during the 3D reconstruction process. Presently, local attenuation is referenced to local density with the reference samples using Eq. (7). The resulting local density is presented as color-coded planar cuts in Figure 6, using the planes defined in Figure 1. The result clearly shows the regions where higher density-values are experimentally observed.

The experimental density distribution shows a surface related artifact, a skin effect, falsely indicating that there was a physically unrealistic ca. 250-300 μm thick low-density layer at the outer surface of the objects. The reason for this bias is that at the surface of the object the air-object interface shows a steep change in the density, which is digitally sampled (compare this to the true spatial resolution of the imaging system, 270 μm). For this transition region, therefore, the measured density values are biased towards lower values and shall be discarded or replaced by the nearest valid piece of data. To prove that this observation is just an imaging artifact, one sample has been broken into two pieces and was re-measured. The result showed that the same surface bias appeared on the freshly broken surface. Finally, the two fragments were tightly reattached and this time no bias was observed at the fracture surfaces. In the authors' opinion,

the skin effect is not detrimental as simulations results can be used to extrapolate density data from a depth where the measurements are reliable and are in agreement with the simulations. However, if the determination of the surface conditions is of special importance; other techniques beyond the presently applied neutron imaging have to be involved.

In a similar manner, the local density after compaction is retrieved from the FE-simulations in planar cuts. The comparison between simulation and measurement is presented as relative density (relative sintered density). The two sets of results are presented in Figure 6 with the same scale for density. Except for the skin effect in the imaging data, the density gradient shows good spatial and numerical agreement. Areas where low density can be expected, for instance in the middle of Plane C far away from the pressing punch, show a similar pattern in simulation and measurement. In the same manner, close to the punch and above the hole, the density is high in both cases as expected. For a quantitative comparison, the local relative density along the lines (a) and (b) as shown in Figure 6, is presented in Figure 7.

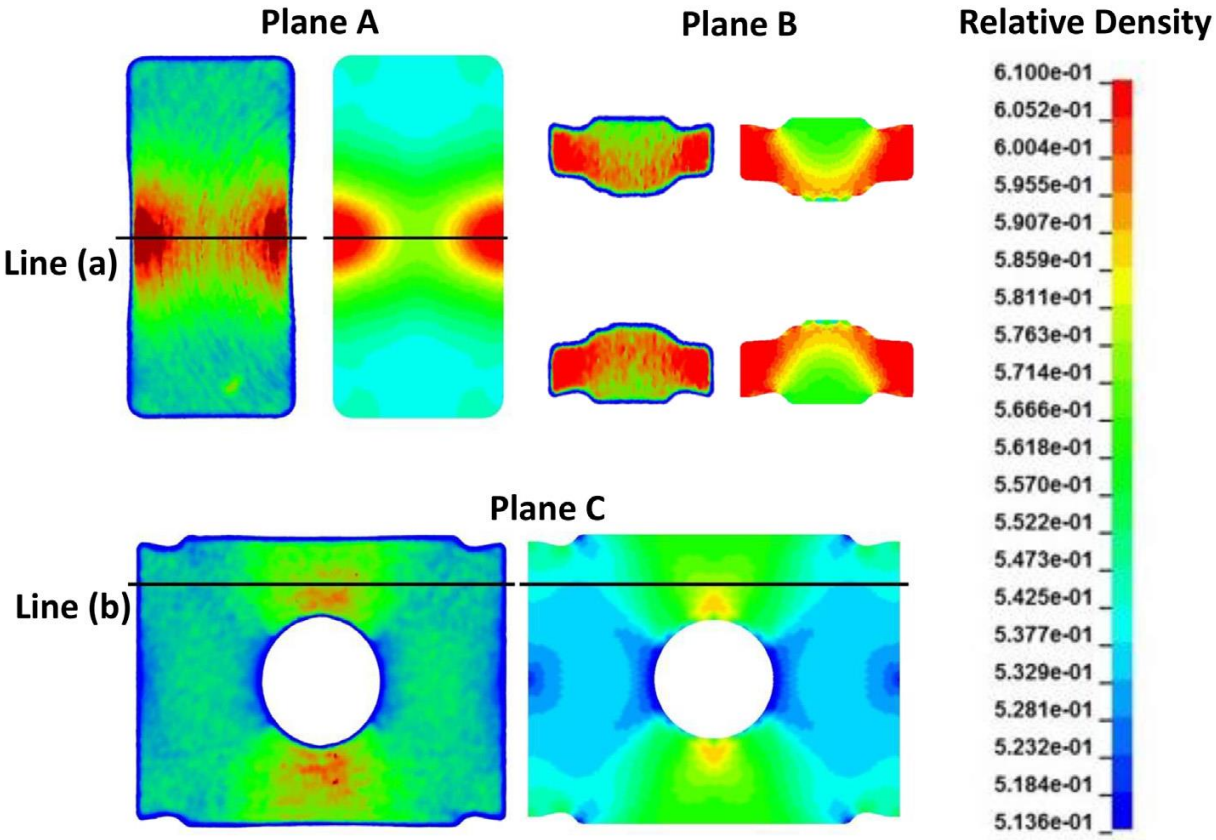

Figure 6: Experimental and simulated relative density distributions at the three planes defined in Figure 1. Measured values are presented in the left views and simulated values in the right views.

. Also, here it can be seen that the pattern is the same and the curves follow each other well. In general, the measurement shows a slightly higher local density. It is believed, however, that this

result is sufficient for material characterization, i.e., determining material constants and functions, in the presently used model for FE-simulations, relying on reverse engineering, as already mentioned earlier.

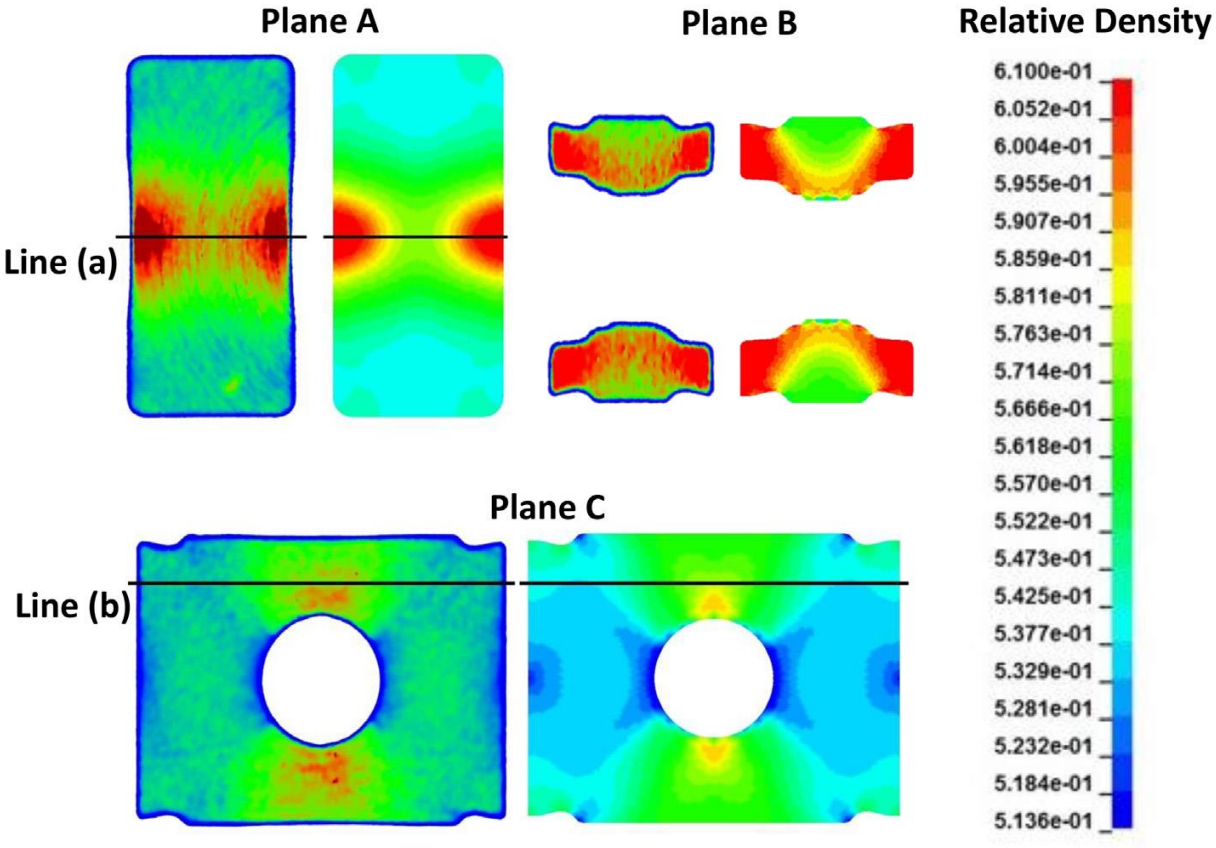

Figure 6: Experimental and simulated relative density distributions at the three planes defined in Figure 1. Measured values are presented in the left views and simulated values in the right views.

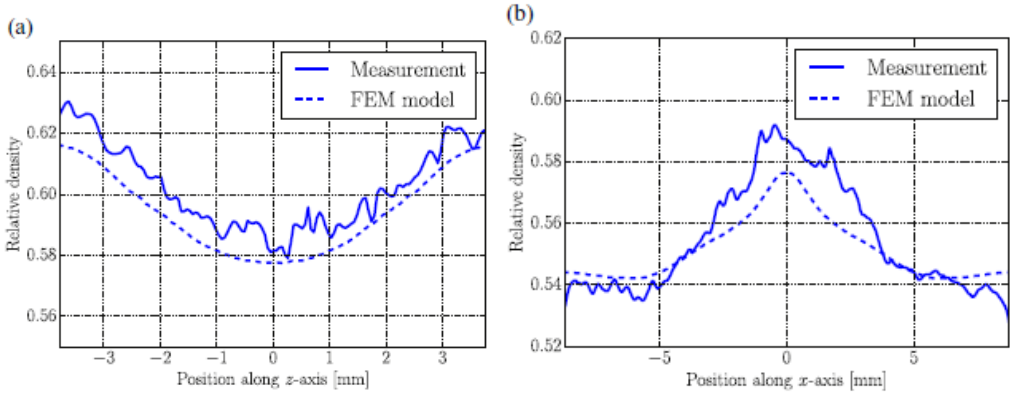

Figure 7: Comparison of measured and simulated relative density along the lines defined in Figure 6. Figure 7 (a) presents data for line (a) and (b) presents data for line (b).

It should be clearly emphasized, in this context, that the density values derived from the FE-simulations cannot be considered as exact, remembering that the FE-analysis includes a number of approximations. In particular, this concerns the explicit values on material constants and functions. Accordingly, the small difference between the measurements and simulations does not necessarily mean that the measurements are biased. However, the close agreement between the two sets of results clearly indicates that the present experimental observations are valuable and that the inherent approximations in the simulations are valid.

For validation of the measurements, the average density in the powder compact, derived from the upscaled 3D attenuation values in Eq. (7), is compared with an average density obtained from the measured weight and the voxel-based total volume from the tomography (note that the so-called water displacement method could be an alternative for validation purposes but this is not attempted here). The comparison shows that the 3D reconstructed local density is 4.3 % too high in absolute densities, and even higher when not considering the biased near-surface layer, as shown in Table 4. For comparison reasons, the average density in the simulation is chosen close to the 3D reconstructed. The reason for this difference in absolute values is believed to mainly be due to the scattering of neutrons. During measurement, it can scatter from the beam, the sample and from ambient structural elements, whereof only effects from the samples are considered here.

Powder compact I	**Density (g/cm^3)**	**Relative density**
Weight density	7.93	50.91 %
Average density in 3D reconstruction	8.26	53.03 %
Average density in 3D reconstruction when outer surface is removed	8.59	54.96 %
Chosen density in simulation	8.54	54.82 %

Table 4: Measured and simulated relative densities of Compact I.

There are small differences in the local density for the three powder compacts marked I to III, where, as shown in **Error! Reference source not found.**, pressing speed and holding time after compaction has been varied. It is plausible to assume that the different fabrication processes of the objects caused the observed changes. Since the distinction in the density gradient is too small to present as cuts of the 3D volume, a cumulative plot of voxel density-value was calculated as shown Figure 8. The number of voxels within a given density range is calculated for each sample and for each range. The graph shows clearly that Compact I differ from the rest, showing a larger volume with low density. This result confirms that the influence from pressing speed on the density gradient is significantly more important than the holding time (related to creep effects), which confirms that creep can be neglected in the present FE simulations, as previously presented in [2].

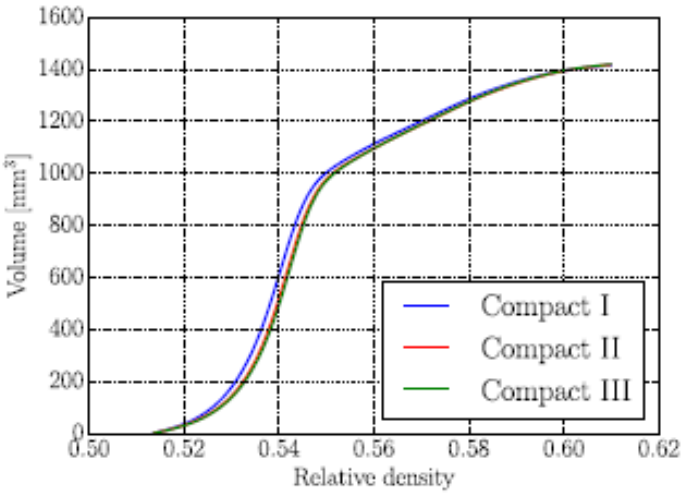

Figure 8: Cumulative histogram of the volumes having a relative density smaller than a given value for the compacts presented in Table 1.

The latter result is, of course, a significant simplification when constitutive modeling is at issue. This feature, together with the fact that the local density variation can be used for inverse modeling, suggests that the outcome of the present study will be very beneficial when it comes to the characterization of hard metal powders and their properties.

6 Conclusion

Measurement of the pointwise density gradient in powder compacts, using polychromatic thermal neutrons, showed good agreement with finite element simulations. The neutron beam at the RAD facility is applicable even for such atomic number main components as tungsten carbide, where X-rays and cold neutrons fail. However, beam hardening, as well as scattering from the hydrogen content of the sample due to the PEG content, must be compensated for. Here beam hardening is taken into account by using a double exponential function, established with a set of homogeneous reference samples, while neutron scattering from it is mitigated by placing the sample 50 mm further from the detector screen. Differences in the density gradients, between samples prepared with different pressing speeds and holding times, could be visualized in a cumulative plot. Presently it was confirmed that the pressing speed affects the density gradient, but the holding time (related constitutively to creep effects) does not. This confirms the conclusions in previous research i.e. that die friction is speed dependent and that creep during relaxation can be neglected. It is believed that the obtained 3D result of the local density is of sufficient quality to be used for validation and characterization, relying on inverse modeling, of a material model, and that it is a useful tool when powder pressing is analyzed.

Acknowledgment

The authors are grateful for the financial support of the SINE 2020 project (Science & Innovation with Neutrons in Europe in 2020, Horizon 2020 grant No 654000), as well as the Project No. 124068 of the National Research, Development and Innovation Fund of Hungary, financed under the K_17 funding scheme. L. Szentmiklósi also gratefully acknowledges the financial support of the János Bolyai Research Fellowship of the Hungarian Academy of Sciences.

References

[1] S. Haglund, J. Ågren, P. Lindskog, B. Uhrenius, Modelling of Solid State Sintering of Cemented Carbides, Sintering Technology (1996) 149-156.

[2] H. Staf, E. Olsson, P. Lindskog, P.L. Larsson, On rate-dependence of hardmetal powder pressing of cutting inserts, Powder Metall. 60 (2017) 7-14.

[3] J. Brandt, On constitutive modelling of the compaction and sintering of cemented carbides, Division of Solid Mechanics, Department of Mechanical Engineering, Linköping University (1998).

[4] A.L. Gurson, Continuum Theory of Ductile Rupture by Void Nucleation and Growth: Part I—Yield Criteria and Flow Rules for Porous Ductile Media, J. Eng. Mater. Technol. 99 (1977) 2–15.

[5] A. Schofield, P. Wroth, Critical state soil mechanics, McGraw-Hill, New York (1968)

[6] F.L. DiMaggio, I.S. Sandler, Material Model for Granular Soils, J. Eng. Mech. Div. 97 (1971) 935–950.

[7] J. Brandt, L. Nilsson, A constitutive model for compaction of granular media, with account for deformation induced anisotropy, Mech. Cohesive-Frictional Mater. 4 (1999) 391–418.

[8] D.C. Andersson, P. Lindskog, P.-L. Larsson, Inverse Modeling Applied for Material Characterization of Powder Materials, J. Test. Eval. 43 (2015) 1005-1019.

[9] P. Lindskog, D.C. Andersson, P.-L. Larsson, An Experimental Device for Material Characterization of Powder Materials, J. Test. Eval. 41 (2013) 504–516.

[10] D.C. Andersson, P.-L. Larsson, A. Cadario, P. Lindskog, On the influence from punch geometry on the stress distribution at powder compaction, Powder Technol. 202 (2010) 78–88.

[11] H. Staf, P. Lindskog, D.C. Andersson, P.-L. Larsson, On the Influence of Material Parameters in a Complex Material Model for Powder Compaction, J. Mater. Eng. Perform. 25 (2016) 4408–4415.

[12] F. Quadrini, E.A. Squeo, Density Measurement of Powder Metallurgy Compacts by Means of Small Indentation, J. Manuf. Sci. Eng. 130 (2008) 034503.

[13] B.J. Briscoe, S.K. Sinha, Density distributions characteristics of green ceramic compacts using scratch hardness, Tribol. Int. 30 (1997) 475–482.

[14] P.R. Laity, R.E. Cameron, A small-angle X-ray scattering study of powder compaction, Powder Technol. 188 (2008) 119–127.

[15] P.R. Laity, R.E. Cameron, A small-angle X-ray scattering study of local variations within powder compacts, Powder Technol. 192 (2009) 287–297.

[16] P.R. Laity, R.E. Cameron, Changes in small-angle X-ray scattering during powder compaction — An explanation based on granule deformation, Powder Technol. 198 (2010) 404–411.

[17] P. Lu, J.J. Lannutti, P. Klobes, K. Meyer, X-ray Computed Tomography and Mercury Porosimetry for Evaluation of Density Evolution and Porosity Distribution, J. Am. Ceram. Soc. 83 (2004) 518–522.

[18] Xiang Zhao, J.L. Rose, Huidong Gao, Determination of density distribution in powder compacts using ultrasonic tomography, IEEE Trans. Ultrason. Ferroelectr. Freq. Control. 53 (2006) 360–369.

[19] H. Staf, E. Forssbeck Nyrot, P.-L. Larsson, On the usage of a neutron source to determine the density distribution in compacted cemented carbide powder compounds, Powder Metall. 61 (2018) 389–394.

[20] J. Schuster, E. Rudy, H. Nowotny, Die “MoC”-Phase mit WC-Struktur, Monatshefte Für Chemie. 107 (1976) 1167–1176.

[21] H. Staf, E. Olsson, P. Lindskog, P.-L. Larsson, Determination of the Frictional Behavior at Compaction of Powder Materials Consisting of Spray-Dried Granules, J. Mater. Eng. Perform. 27 (2018).

[22] B.P. Bewlay, Consolidation dynamics of tungsten powder during dry bag cold isostatic pressing, Int. J. Refract. Met. Hard Mater. 11 (1992) 165–174.

[23] Z. Kis, L. Szentmiklósi, T. Belgya, M. Balaskó, L.Z. Horváth, B. Maróti, Neutron Based Imaging and Element-mapping at the Budapest Neutron Centre, Phys. Procedia. 69 (2015) 40–47.

[24] N. Chankow, Neutron Radiography, in: Nondestruct. Test. Methods New Appl., InTech (2012).

[25] E. Lehmann, P. Vontobel, N. Kardjilov, Hydrogen distribution measurements by neutrons, Appl. Radiat. Isot. 61 (2004) 503–509.

[26] I.S. Anderson, R.L. McGreevy, H.Z. Bilheux, Neutron imaging and applications : a reference for the imaging community, Springer (2009).

[27] E.H. Lehmann, A.P. Kaestner, 3D Neutron Imaging, in: Encycl. Anal. Chem., John Wiley & Sons, Ltd, Chichester, UK (2009).

[28] J. Schindelin, I. Arganda-Carreras, E. Frise, V. Kaynig, M. Longair, T. Pietzsch, S. Preibisch, C. Rueden, S. Saalfeld, B. Schmid, J.-Y. Tinevez, D.J. White, V. Hartenstein, K. Eliceiri, P. Tomancak, A. Cardona, Fiji: an open-source platform for biological-image analysis, Nat. Methods. 9 (2012) 676–682.

[29] Octopus Analysis | Octopus Imaging Software

[30] VGSTUDIO MAX - Products - volumegraphics.com

[31] A. Kaestner, Kiptool for Windows, (2018).

[32] J. Alles, R.F. Mudde, Beam hardening: Analytical considerations of the effective attenuation coefficient of x-ray tomography, Med. Phys. 34 (2007) 2882–2889.

[33] J.O. Hallqvist, LS-Dyna Theory Manual, Livermore (2006).

[34] LS-Dyna Keyword User's Manual II, Material Models, Livermore (2016).

[35] P. Samuelson, B. Bolin, Experimental studies of frictional behaviour of hard metal powders sliding on cemented carbide walls, Scand. J. Metall. 12 (1983) 315–322.